Journal of Materials Chemistry A

PAPER

View Article Online
View Journal | View Issue

Cite this: J. Mater. Chem. A, 2018, 6, 7500

pH-Dependence in facet-selective photo-deposition of metals and metal oxides on semiconductor particles†

Yuxi Guo,‡[ac] Igor Siretanu,‡*[b] Yihe Zhang,*[a] Bastian Mei,[c] Xiaowei Li,[a] Frieder Mugele,[b] Hongwei Huang*[a] and Guido Mul*[c]

Received 24th January 2018
Accepted 22nd March 2018

DOI: 10.1039/c8ta00781k

rsc.li/materials-a

Facet-engineering and the deposition of co-catalysts lead to significant improvement in efficiency of semiconductors in photocatalytic applications. Here, we demonstrate, using the specific example of bismuth-oxy-bromide (BiOBr) particles, that facet-selective, photo-induced reductive or oxidative deposition of co-catalysts onto plate-like semiconductor particles is strongly pH-dependent. High resolution atomic force microscopy and spectroscopy measurements demonstrate that the effect of pH is caused by a reversal of the surface charge of the [001] facets upon increasing pH from 3 to 9 (isoelectric point ≈5), while the side facets become increasingly negatively-charged. We discuss the effect of facet-surface-charge on particle distributions by band-bending, favoring either electron transfer and metal deposition, or hole transfer and metal-oxide deposition. This finding opens up new ways to design highly effective, photocatalytic composite architectures, containing spatially separated catalytic particles of multiple compositions.

Introduction

Semiconductor-based photocatalysis can address some of the most important challenges of modern industrialized societies, namely (i) the replacement of fossil fuels by solar fuels, and (ii) the purification of water and air by light induced conversion of toxic hydrocarbons into CO_2 and H_2O.[1–5] For photocatalysts to be efficient, photo-generated charge carriers need to be effectively separated and transferred to the reactants.[6–10] Optimization of crystal size and crystallinity, addition of a co-catalyst, and crystal facet engineering have been used to reduce probability of electron–hole recombination, and to improve photocatalytic activity.[9,11–17] Crystal facet engineering is considered to be particularly promising,[13,18–21] since recent investigations have identified the dependence of photocatalytic performance on the nature of exposed facets of crystals of BiOBr,[22–24] $BiVO_4$,[25,26] TiO_2,[27,28] WO_3,[29,30] $SrTiO_3$ (ref. 31 and 32) and others.[13,14,24] Facet-selective separation of electrons and holes can be monitored directly by spatially resolved surface photovoltage spectroscopy (SRSPS) in vacuum,[33] or indirectly by *ex situ* microscopy-analysis of facet-selective photo-deposition of nanoparticles from aqueous solution, formed either by reduction or by oxidation of precursor ions. From these studies it was postulated that reductive deposition of metallic Ag, Au, and Pt occurs preferentially on electron-accumulating facets, whereas the oxidative deposition of MnO_x and PbO_2 takes place on hole-accumulating facets.[10,24,25]

Generally, the explanation of a facet-specific, high concentration of charge carriers is based on facet-dependent levels of valence band maxima and conduction band minima, which can be calculated by density functional theory (DFT).[25,32,34] While qualitatively successful in many cases, such explanation disagrees with several studies in which facet-selective deposition was not achieved. In addition, such purely solid state-based reasoning fails to explain the dependence of photocatalytic reactions on the composition of the ambient electrolyte.[35–42] For instance, oxygen evolution on TiO_2 is known to strongly depend on pH, and can be affected by the presence of adsorbing species like Li^+, Na^+ and K^+, indicating charge carrier redistribution near the semiconductor–electrolyte interface is significant.[38,41,43–50] Similarly, it was shown that the quantum efficiency of p-GaN nanowires can be enhanced by almost two orders of magnitude by tuning surface band bending *via* the pH of the applied electrolyte.[45,46] Besides levels of valence band maxima

[a]Beijing Key Laboratory of Materials Utilization of Nonmetallic Minerals and Solid Wastes, National Laboratory of Mineral Materials, School of Materials Science and Technology, China University of Geosciences, Beijing 100083, China. E-mail: zyh@cugb.edu.cn; hhw@cugb.edu.cn

[b]Physics of Complex Fluids Group, MESA+ Institute, Faculty of Science and Technology, University of Twente, PO Box 217, 7500 AE Enschede, The Netherlands. E-mail: i.siretanu@utwente.nl

[c]Photocatalytic Synthesis Group, MESA+ Institute for Nanotechnology, University of Twente, P.O. Box 217, 7500 AE Enschede, The Netherlands. E-mail: g.mul@utwente.nl

† Electronic supplementary information (ESI) available: Additional characterization including XRD, AFM, SEM, and XPS, schematics of the BiOBr structure, and illustration of the electric double layers at the semiconductor/aqueous electrolyte interface. See DOI: 10.1039/c8ta00781k

‡ These authors contributed equally to this work.

and conduction band minima, other factors apparently need to be taken into consideration, such as electrolyte composition, surface charge, ion adsorption, surface defects, and surface hydration, to explain the experimental observations of facet-specific charge concentrations.

We have taken the following approach to investigate the impact of electrolyte composition on facet-selective photodeposition, and to reveal the underlying mechanism behind this intriguing phenomenon.

First, the semiconductor BiOBr was selected as model system. Bismuth oxybromide (BiOBr) and the entire bismuth oxyhalide (BiOX, where X = Cl, Br or I) family has attracted considerable interest in the community studying photocatalysis, due to excellent photocatalytic activity, a readily tunable electronic structure, and a high chemical stability under visible light irradiation in a broad pH range of solution.[51–55] Specifically, BiOBr has a band gap of 2.7 eV,[52,56,57] while the visible-light-driven (VLD) photocatalytic performance of BiOBr is structure-dependent.[22–24,51–57] Finally the synthesis of faceted BiOBr particles is straightforward.

Second, we used *in situ* Atomic Force Microscopy (AFM) in combination with photo-induced reductive deposition of metals (Au, Pt), or oxidative deposition of metal oxides (MnO_x, PbO_2), to demonstrate that facet-selective concentrations of charges and deposition of particles onto BiOBr is strongly pH-dependent. The effect of pH is caused by a reversal of the surface charge of the [001] facets upon increasing the pH from 3 to 9 (isoelectric point 5), while the side facets become increasingly negatively-charged upon increasing the pH of the solution. Our observations suggest that facet-specific, pH-dependent variations of the surface charge give rise to a pH-dependent facet selectivity of redox reactions beyond the well-known dependence on the intrinsic band structure of the semiconductor. We expect that this principle should be applicable for a wide range of semiconductor materials.

Experimental

Synthesis of bismuth oxy bromide (BiOBr)

A modified hydrothermal procedure was employed to prepare plate-like BiOBr crystals.[22,58] Briefly, 0.975 g of $Bi(NO_3)_3 \times 5H_2O$ (Sigma-Aldrich, puriss., ≥99%) was mixed with 50 ml of an aqueous solution containing 0.238 g of KBr (Sigma-Aldrich, ≥99.0%).[59] The resulting suspension was heated at 120 °C for 24 h in a 100 ml Teflon-sealed stainless steel autoclave and subsequently air cooled to room temperature. After centrifuging, the obtained powder was washed three times with ethanol and deionized water, respectively, and finally dried in air at 60 °C.

Photo-deposition of noble metals and/or metal oxides

A solution of H_2PtCl_6 (Aldrich, 8 wt% in H_2O), $HAuCl_4$ (Sigma-Aldrich, ACS reagent, ≥49.0% Au basis), $MnSO_4 \cdot H_2O$ (Sigma-Aldrich, puriss., ≥99%), or $Pb(NO_3)_2$ (Sigma-Aldrich, puriss., ≥99%) was used as precursor for the photo-deposition of Pt, Au, PbO_2 or MnO_x respectively. For the photo-deposition experiments, 200.0 mg of BiOBr and a calculated amount of metal precursor (H_2PtCl_6, $HAuCl_4$, $MnSO_4$ or $Pb(NO_3)_2$), corresponding to a theoretical loading of 3 wt%, were suspended and dissolved in 50 ml of deionized water. The suspension was first stirred in the dark for 1 h to achieve an adsorption–desorption equilibrium and subsequently irradiated for 1 hour with a 50 W HBO mercury lamp (Zeiss, 46 80 32 – 9902). In case of photodeposition of Pt, 8 ml of methanol were added to the solution prior to illumination. Finally, the modified BiOBr materials were obtained by thorough washing with deionized water and ethanol and subsequent drying in air at 60 °C.

Impregnation of BiOBr with metal or metal oxide particles was performed according to the literature[25] by suspending 0.20 g BiOBr and a calculated amount of metal/metal oxide precursors (3 wt%) in 50 ml deionised water. During continuous stirring, the suspension was kept at 70 °C until a dry powder was obtained (approx. 10 h). Subsequently, the powder was calcined at 350 °C for 2 h.

Characterization

Powder X-ray diffraction (XRD) patterns of all products were recorded using a Bruker D8 Advance powder X-ray diffractometer using monochromatic Cu Kα (λ = 0.15406 nm) radiation. The morphologies and microstructures of the as-prepared samples were analyzed by high-resolution scanning electron microscopy (HRSEM). Diffuse reflectance ultraviolet-visible spectra (DRS) of the as-prepared particles were measured using a UV-vis spectrophotometer (PerkinElmer Lambda 35) referenced to the reflectance of $BaSO_4$. The chemical composition and valence state of the deposited nanoparticles were analyzed using a VGMK II X-ray photoelectron spectrometer (XPS), and the spectra were referenced to the adventitious C 1s peak at 284.6 eV. Mott–Schottky experiments were carried out on a three-electrode electrochemical setup (potential: −0.8 V to 0.8 V, frequency: 100 Hz) using 0.1 M Na_2SO_4 solution (pH = 5.91) as electrolyte. FTO glass was coated with the BiOBr samples, and a platinum electrode and saturated calomel electrode (SCE) were used as counter and as reference electrode, respectively.

The zeta (ζ) potential and the hydrodynamic radius of the BiOBr particles were characterized with a Zetasizer Nano ZS dynamic light scattering system, using a 633 nm laser (Malvern Instruments, Malvern, UK) and sealed polystyrene containers. Prior to the experiment, the diluted suspension (0.005 g per 10 ml MQ water) of particulate sample was sonicated for 5 min to obtain a well-defined, non-flocculated starting state. The required pH value of the samples was adjusted by adding an appropriate amount of 0.1 M HCl or 0.1 M NaOH.

After a thermal equilibration time of 120 s at 25 °C electrophoretic measurements were taken in a voltage range of 5 V. The electrophoretic mobility was calculated from the average particle velocity and the electric field strength, based on the measured ion current and the conductivity of the suspension. Finally, ζ potentials were derived from the electrophoretic mobilities using the Smoluchowski approximation using the Malvern Instruments Software Version 6.01.

Atomic force microscopy measurements

AFM measurements were conducted using a Cypher ES (Asylum Research, Oxford Instruments, Santa Barbara, CA, USA), except for the results presented in Fig. 2a, which were obtained on a dimension Icon AFM (Bruker Corporation). All measurements were performed with the cantilever/tip and the sample fully immersed in the solution. The measurements with the Cypher were thermally stabilized (±0.1 °C) and the tip oscillation was driven photo-thermally for greater stability using either Arrow UHF-AUD (Nanoworld, Neuchatel, Switzerland) cantilevers with a spring constant of 3–5 N m^{-1} or MikroMash NSC36/Cr–Au BS cantilevers with a spring constant of 0.6–1 N m^{-1}. Tips and substrates were cleaned prior to the experiments by excessive rinsing with isopropanol, ethanol and water followed by plasma cleaning (PDC-32G-2, Harrick Plasma) for 20–25 min. The AFM was operated in amplitude modulation mode with small working amplitudes A between 0.5 nm and 1.5 nm and a set-point ratio $A/A_0 > 0.8$, where A_0 is the free vibration amplitude of the tip away from the interface. In combination with ultrasharp tips, these conditions enable atomic resolution imaging. If not otherwise stated, BiOBr particles were immobilized on Pt substrates.

Quantification of the surface charge (potential) of the basal plane of BiOBr particles is based on the conversion of measured AFM amplitude and phase signals into forces.[60,61] Subsequent conversion of the resulting force–distance curves into surface charge densities and potentials, involves the numerical solution of the Poisson–Boltzmann theory, including charge regulation boundary conditions for the electrostatic forces, and van der Waals interactions.[60–62] It should be pointed out that the charge of the tip for each testing condition should be measured, as this is pH and electrolyte dependent. This is done by measuring and fitting silica–silica interactions (silica tip–water–silica substrate) for each pH condition. Fitting the interaction force between the silica AFM tip and a silicon substrate oxidized in air to produce amorphous SiO_2 (not shown here), yields the following charges for the tip: at pH 3, $\sigma = -0.0103e$ nm^{-2}; at pH 6, $\sigma = -0.11e$ nm^{-2}; at pH 9, $\sigma = -0.154e$ nm^{-2}. The low value measured at pH 3 agrees well with the point of zero charge of silica, which has been reported to be close to 3. Once the charge of the tip surface is known, the charge of the BiOBr basal surface can be quantified. The lower limit for the fitting range was set to 2 nm to minimize the influence of short range forces such as hydration forces that are not included in the theoretical model. The upper boundary was set to 25 nm above the surface, at which the interactions are negligibly small. The geometry of every AFM tip was characterized after the experiment by high resolution SEM, to ensure reproducibility.

Results and discussion

Structural characterization of BiOBr

BiOBr particles were prepared by hydrothermal synthesis, see the Experimental procedures.[22,58] The particles show a certain degree of polydispersity, both in size and shape. They display characteristic widths of 1–2 μm and a thickness ranging from several tens, to a few hundreds of nanometers, as seen in both scanning electron microscopy (SEM) (Fig. 1 and S1a†), and Atomic Force Microscopy (AFM, Fig. 2 and S1c†). Considering the plate-like morphology of the crystals, and their assumed

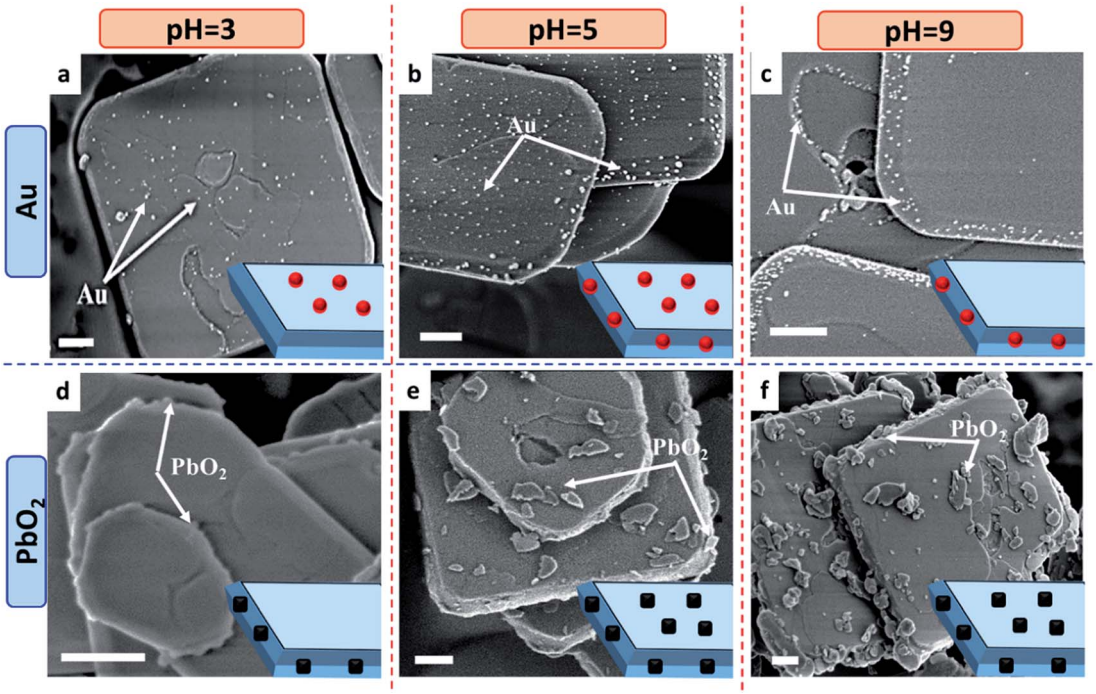

Fig. 1 SEM images of BiOBr nanoparticles. SEM images of BiOBr showing pH-dependent geometrical deposition of Au or PbO_2 nanoparticles. Au/BiOBr at (a) pH 3; (b) pH 5; (c) pH 9; PbO_2/BiOBr at (d) pH 3; (e) pH 5; (f) pH 9. The scale bar always corresponds to 200 nm.

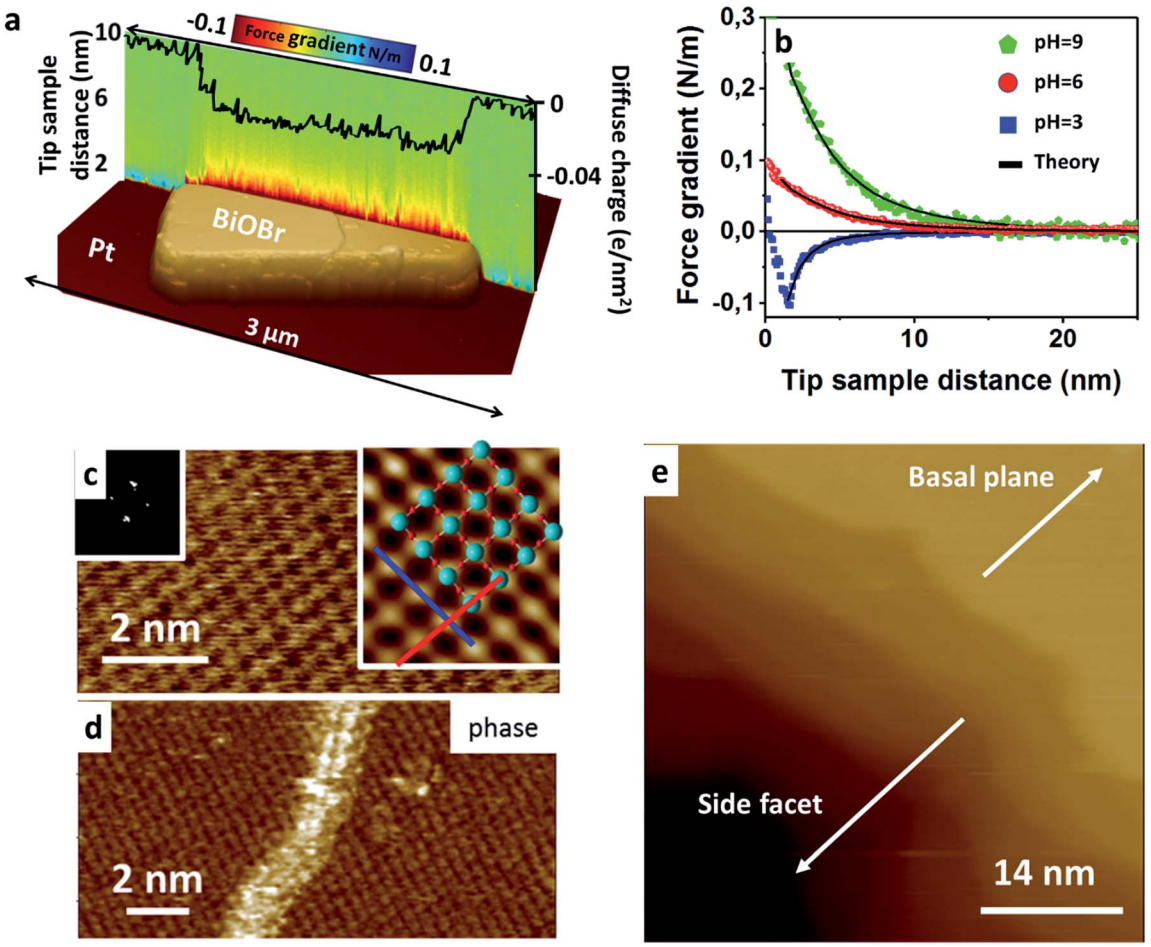

Fig. 2 Atomic force microscopy (AFM) of BiOBr nanoparticles. (a) Combined 2D force field images, obtained by measuring 300 single force-*versus*-distance curves along a line in the *x* direction over a plate-like BiOBr sample in 10 mM aqueous NaCl at pH 6. Blue forces are indicative for attractive interactions with the tip, whereas red forces indicate negative surface charges. The black line superimposing the 2D force field represents the resulting surface charge profile after analysis of 300 tip–sample interaction forces. (b) Tip sample interaction forces on BiOBr in 10 mM NaCl solution at pH 3, 6, and 9, respectively. Dotted lines represent the experimental curves and solid lines are the theoretically fitted force curves using the DLVO theory and a charge regulation boundary condition. (c) AFM topographic image at the atomic scale of a BiOBr basal plane in contact with ultrapure de-ionised water. Insets: zoomed and Fourier-filtered view with the superimposed crystallographic lattice (right); 2D fast Fourier transform of the image (left). See Fig. S2† for more details. (d) Atomic resolution phase image around a step-edge. The strong phase contrast illustrates strongly different local interaction forces. For topography: see Fig. S2.† (e) Atomic resolution topography image close to the edge of the particle or side plane, displacing a non-periodic structure and steps. For the corresponding phase see Fig. S2e.†

tendency to align normally to the sample axis, the diffraction pattern (Fig. S1b†) suggests that the basal facet is [001], consistent with atomically resolved AFM images (Fig. 2c, d and S2†). The more or less regular sides consist primarily of [102] facets.[22,23,63] Similar to earlier studies of WO_3 nano-platelets and various types of natural clays,[61,64] the surface of the BiOBr particles consists of atomically smooth [001] terraces separated by atomic steps, which typically increase in density upon approaching the edge of a particle, as shown in Fig. 2d and S2.† Close to the boundary between the basal plane and the side plane, we typically find a region with a width of a few tens of nanometers (approx. 30% of side facet width) that contains many defects and steps (Fig. 2d and S2h, e†). In all cases, measurements of the surface charges of the basal planes are taken sufficiently far away from any edge to guarantee that they reflect only basal plane properties.

UV-vis spectra (Fig. S3†) indicate that BiOBr exhibits an extended absorption into the visible region of the light spectrum, in agreement with the literature.[53,65] Mott–Schottky measurements confirm that BiOBr is an n-type semiconductor (Fig. S3c†).[22,58,66]

Photo-deposition at variable pH

To probe facet-preferential charge concentrations upon illumination, we performed photo-deposition experiments using both cationic and anionic precursors. Reductive photo-deposition of Au and Pt was carried out using $HAuCl_4$ and H_2PtCl_6 solutions in the absence (Au) or presence of methanol (Pt). In the absence of methanol, Pt deposition on the BiOBr surface was not observed within the usual deposition time (1 hour). Contrary to Au, the relatively small driving force (low potential difference between the VB of BiOBr and the redox-potential of the Pt-

precursor) might explain the lack of Pt deposition in the absence of methanol. Because of the additional complexity of adding methanol to the solution, we mainly focus the discussion of the results on the deposition of Au. Additionally, photo-oxidative deposition of PbO_2 and MnO_x was performed from salt solutions containing Pb^{2+} and Mn^{2+}, see details provided in the Experimental paragraph. For metal, and metal-oxide nanoparticles, photo-deposition was carried out at variable pH (3, 5, 7, 9). The pH range did not significantly affect the composition of the Au precursor, *i.e.* $AuCl_4^-$ is present in solution at all pH values.[67] The precursor solution contained the equivalent amount of a (theoretical) loading of 3 wt%, sufficient to easily characterize the functionalized materials by scanning electron microscopy (SEM).

SEM imaging after photo-deposition reveals pH-dependent facet-selective deposition of metal and metal oxides, as shown in Fig. 1 (and S4†). At pH 3, we observe an overall limited deposition of Au (and Pt), preferentially on the [001] facet. Under the same conditions, PbO_2 (and MnO_x) particles are preferentially deposited on the side facets. Similar results were obtained when H_2SO_4 (otherwise HCl) was used to adjust the pH of $MnSO_4$ solutions (see Fig. S4p†). This experiment rules out the possibility that the photodeposition process is affected by specific adsorption of Cl^- ions.

To verify that the observed facet-selective adsorption is indeed photo-induced rather than, *e.g.*, triggered by preferential adsorption of the precursors from the solution, we performed conventional impregnation tests in the absence of light. Subsequent SEM imaging indicates random deposition on every facet, see Fig. S6.† This confirms the photo-induced character of facet-selectivity shown in Fig. 1 and S4.†

Upon increasing the pH of the solution to 5, 7, and 9, the photo-deposition pattern gradually changes. For reductive deposition, Au (and Pt) particles are found on every facet for intermediate pH values and only on the side (lateral) or [102] facets for pH 9. *I.e.* the facet-selectivity of the metal reduction reaction reverses from the [001] facets at low pH to the side facets at high pH. For PbO_2 (and for MnO_x), the changes in selectivity are similarly drastic. While the oxides are exclusively deposited on the lateral facets at low pH, oxide-particles with a rather irregular shape and size distribution also appear on the [001] facets at intermediate and elevated pH. Simultaneously, oxide is still being deposited on the side facets, thus leading to a loss of facet selectivity for this oxidative reaction. The integrity and crystallinity of BiOBr was not affected by the pH of the solution in the range of 3–9, nor during deposition by dark impregnation, nor during photodeposition of metal(oxide), as can be seen from SEM images and XRD analysis (Fig. S5 and S7†). We believe the apparent irregular shape of the particles after PbO_2 deposition at pH 9 is due to the extensive amount of PbO_2 formed.

To quantify the amount and the oxidation state of photo-deposited particles as a function of solution pH, we carried out XPS measurements after photo-deposition, shown in Fig. S8.† For samples modified by photo-oxidation, XPS confirmed the presence of PbO_2 and MnO_x in different quantities (in agreement with SEM), but similar oxidation state. In particular, high quantities of PbO_2 were observed after deposition at pH 9.

For the Au- and Pt-particles obtained by photo-reduction of $PtCl_6^{2-}$ and $AuCl_4^-$,[68] the characteristic 4f signals shift to higher binding energies as a function of increasing pH, indicating that the average oxidation state increases. Similar differences in oxidation states between Pt and Au were also observed by Li *et al.* and might be due to a relatively high degree of hydroxylation of the Pt and Au precursors.[25] In addition, this increase in oxidation state might be related to a decrease in the reduction rate of $PtCl_6^{2-}$ and $AuCl_4^-$, the consequence of a lower availability of photo-generated electrons on the surface of BiOBr at high pH (for further information about XPS, see ESI†).

The facet selectivity observed at pH 3 is consistent with previous reports and with DFT calculations (see ESI† for details of the calculations). The band structure calculated by DFT shows that the conduction band minimum of the [001] facet is at lower energy than of the [102] facet (Fig. S9a†). *Vice versa*, the valence band maximum of the [102] facet is at higher energy than of the [001] facet. Hence, the DFT calculations suggest that electrons should accumulate on the [001] facets to preferentially induce reduction reactions, while holes should accumulate on the [102] facets to induce oxidation reactions. Yet, this is only consistent with the experimental observations at low pH, while the behavior at high pH is not in agreement with the calculated band alignment. Clearly, explaining the photo-catalytic behavior based on band-structure calculations, is insufficient to capture the pH dependence of the response.

Surface charge of nanoparticles

To rationalize the observed pH dependence of photocatalytic deposition, we characterized the surface charge of the BiOBr nano-particles as a function of pH in two different manners, as illustrated in Fig. 2 and 3. First, we found that the average surface charge $\bar{\sigma}$, as determined using standard zeta potential measurements, displayed an overall negative surface charge throughout the entire pH range from 1.5 to 11, see Fig. 3a. While the magnitude of the charge decreased as a function of decreasing pH, the isoelectric point (IEP) of the entire particle clearly lies below pH 1. Second, we extracted the local surface charge of the [001] facet from measurements of (dynamic) force–distance curves using *in situ* AFM at variable pH; see Experimental for details on AFM measurements. AFM provides information about the charge density in the diffuse part of the electric double layer, similar to those obtained by ζ-potential measurements.[62]

At pH 6 and 9, force–distance curves obtained along a one-dimensional cross section of BiOBr nanoparticles display increasingly repulsive forces upon approaching the surface, as illustrated by the red color-code in Fig. 2a and the positive force gradients in Fig. 2b (see Fig. S10† for more details). Upon decreasing the pH to 3, however, the force gradient becomes negative and the AFM tip experiences an attractive force towards the BiOBr surface. Since the AFM tip, which is made of oxidized Si, is negatively charged between pH 3 and 9, the reversal of the sign of the force upon lowering the pH qualitatively indicates a reversal of the surface charge. Quantitative analysis of the force curves is performed by combining standard Derjaguin–

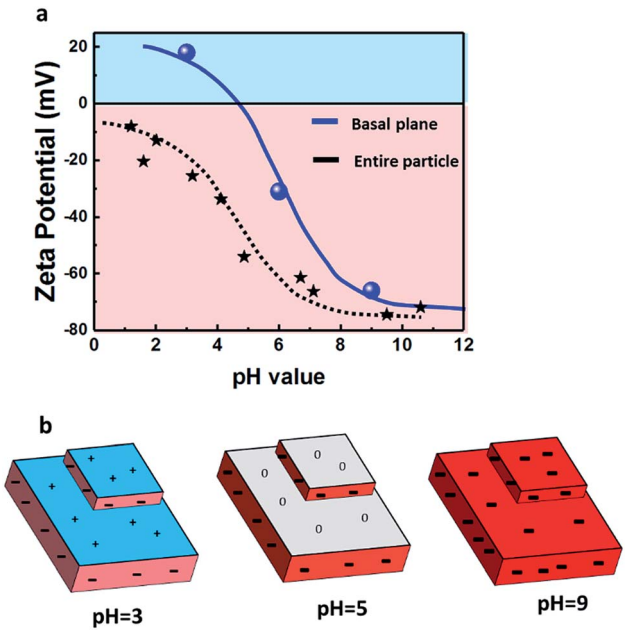

Fig. 3 Surface potential at the aqueous electrolyte–BiOBr nanoparticle interface. (a) Zeta potential as a function of pH for BiOBr nanoparticles (black stars). Diffuse layer potential measured by AFM as a function of pH for BiOBr basal planes (blue dots). (b) Schematic view of BiOBr platelets and their anisotropic charging behavior. The faces (basal planes) exhibit very different amphoteric, pH-dependent behavior. The respective charging conditions may cause changes in positions of electronic band edges and selective/different interaction with $AuCl_4^-$ or $PtCl_6^{2-}$ anions and/or cations such as Pb^{2+} or Mn^{2+} with basal planes and edges.

Landau–Verwey–Overbeek (DLVO) theory in combination with a charge regulation boundary condition during the numerical solution of the Poisson–Boltzmann equation with a surface complexation model.[62,69] Fitting the theoretical curves to the experimental data (black lines in Fig. 2b) yields values of the diffuse layer potential Ψ and (diffuse layer) surface charge density σ_s for pH 3: $\Psi = +18$ mV; $\sigma_s = +0.27e$ nm^{-2}; for pH 6: $\Psi = -31$ mV; $\sigma_s = -0.047e$ nm^{-2}; for pH 9: $\Psi = -66$ mV; $\sigma_s = -0.103e$ nm^{-2}. The [001] facet thus reverses its charge between pH 3 and pH 6. A smoothed interpolation of the data suggests an IEP of approximately 5, see Fig. 3a. Taking into account the approximate area ratio $A_{\{001\}}/A_{\{102\}} \approx 4:1$, this implies that the actual charge density of the negatively charged side facets is (substantially) more negative than the average ζ potential measurements suggest. Based on the combination of AFM and ζ potential measurements we can thus derive the following picture: at low pH, [001] facets are weakly positively charged and lateral facets are weakly negatively charged; at intermediate pH the [001] facets are weakly negatively charged, and side facets strongly negatively charged. Finally, at high pH all facets are rather strongly negatively charged, see Fig. 3b.

The electric field due to the negative charges on the solution side creates a barrier that repels the photo-excited electrons from the surface and thereby gives rise to an electron depletion (increased hole concentration) layer. As a consequence, the electronic bands bend upwards and a positive space charge region (SCR) will exist beneath the surface,[36–40] as depicted in Fig. S11.† The presence of band bending can significantly reduce the electron–hole pair recombination rate and enhance the migration of one type of charge carrier (electron or hole) to the semiconductor surface, which may enhance the electron/hole mediated reaction on the semiconductor surface and the photocatalytic performance by orders of magnitude.[45,46]

Correlating intrinsic surface charge and photo-induced charge migration

As already mentioned in the introduction, an explanation of charge migration on the basis of facet-dependent band positions, does not sufficiently consider phenomena at the interface of the electrolyte and the semiconductor. While correctly predicting the observed migration of electrons to the [001] facets and of holes to the side facets at low pH, such assumption does not include the role of adsorbed water and the adjacent electrolyte (see Fig. S11†), and therefore does not reproduce the pH dependence of facet selectivity reported here. Based on our experimental observations, we conclude that pH-dependent variations of the surface charge of the solid–liquid interface and the associated bending of the electronic bands are primarily responsible for the observed changes in the photo-deposition behavior.

The basic scenario is sketched in Fig. 4. At low pH, the surface charge on both [001] and side facets is small. Hence, the effect of the chemically induced surface charge on the electronic band structure is weak. At the same time, at pH 3, the two surfaces (basal planes and side facets) are charged with opposite signs.

Therefore, electrons preferentially accumulate on the [001] facet due to the intrinsic downward band bending.[36] Likewise, increased hole concentrations occur at the side facets because of the upward bending of the valence band, Fig. 4a. Hence, we expect reduction reactions to take place preferably on the [001] and oxidation reactions on the side facets. Fig. 4d shows this is in agreement with the experiments. Upon increasing the pH, however, the inversion of the surface charge on the [001] facets first flattens the bands (at intermediate pH) and eventually reverses their curvature at high pH, Fig. 4b and c. As a consequence, electrons are no longer attracted towards the [001] surface and are hence no longer available for the reduction of metal cations. Eventually, the reduction reaction completely ceases until metal is no longer deposited. In practice, we still find occasional metal clusters on the [001] facets, see Fig. 2b. Their location, however, is usually associated with defects on the surface such as (arrays of) atomic steps that are present in higher density close to the side facets, as evident from detailed AFM studies. Such defects (see Fig. S2†) act as efficient electron sink.[70,71] From the deposition of Pt and Au on the highly negatively charged side facets at high pH, we conclude that such defect-mediated charge trapping can take place, despite unfavorable electrostatically induced band bending, as illustrated in Fig. 4e. The defects are more likely to be on the side facets, because of the layered structure of BiOBr, which is composed of $[Bi_2O_2]$ slabs, interleaved with double halogen atom slabs along the [001] direction.

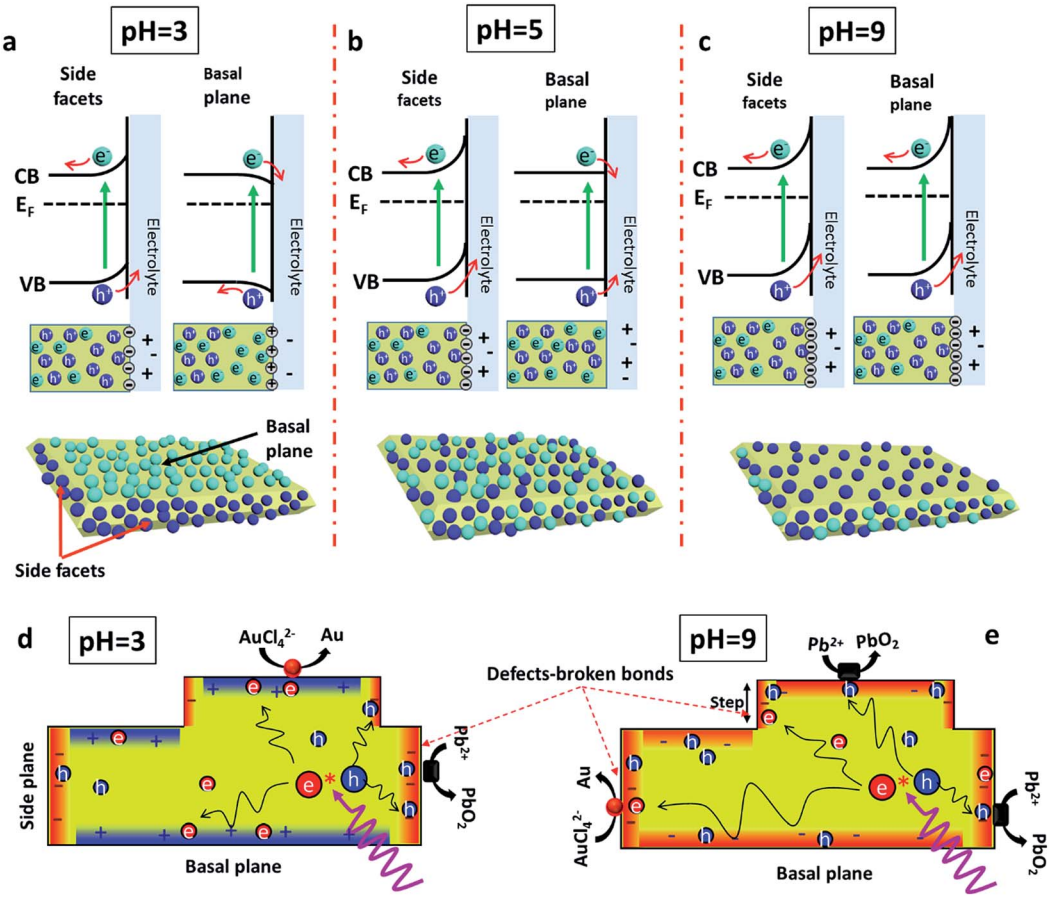

Fig. 4 Schematic illustration of the energetic situations at the BiOBr/electrolyte interface. Top: Schematic band diagrams (in dark conditions) of the side facets and basal plane in contact with water at pH 3 (a), pH 5 (b), and pH 9 (c), and proposed positive (dark blue, holes) and negative (light blue, electrons) charge distributions upon illumination, which are in agreement with metal, or metal oxide deposition, respectively. Two representations of charge migration are shown as well, at pH 3 (d) and pH 9 (e). At pH 3, electrons and holes are migrating to [001] and [102] facets, respectively, to compensate for intrinsic positive and negative charge of these facets. At pH 9, holes are migrating to [001] and [102] facets to compensate for the highly negative intrinsic charge of these facets. Electrons are moving towards defect sites, such as vacancies, steps and the side facets.

The loss of the facet-specificity of the Mn^{+} and Pb^{2+} oxidation upon increasing pH is also consistent with the reversal of the surface charge at the [001]. The negative curvature of the bands upon approaching the [001] surface repels holes at low pH and thereby prevents the oxidation reaction. At higher pH, however, the bands are flattened and eventually positively curved. Hence, the surface becomes attractive to holes and deposition of oxidized PbO_2 and MnO_x becomes possible, in agreement with Fig. 1e and f. Due to this favorable band bending of the basal planes and the side facets, larger quantities of metal oxides are deposited at alkaline pH, in agreement with the XPS results (Fig. S6†).

The combination of AFM and SEM provides clear evidence of the influence of surface charge and surface defects on the facet-selective photodeposition of metals and metal oxides. Even though our analysis of facet dependent reactivity goes beyond the current state-of-the-art, the role of various parameters, such as ions in solution or the presence of sacrificial reagents has not been addressed. In our ongoing work we particularly focus on the effect of more complex varieties in electrolyte composition on geometrical particle distributions, and extend our work to other semiconductor compositions.

Conclusions

In summary, our combined SEM photo-deposition and *in situ* AFM surface charge measurements reveal that the increased concentrations of photo-generated charge carriers at different facets of BiOBr, follows the expectations based on facet-dependent band position derived from DFT calculations, only at low solution pH, where the charge density of the semiconductor–electrolyte interfaces is weak. At higher pH, where the chemically induced surface charge density on the side facets becomes increasingly negative, and the one on the [001] basal plane reverses sign, surface charge-induced band bending needs to be taken into account to explain the experimentally observed photo-deposition patterns. The conscious use of facet-specific surface chemistries and charging characteristics thus allows to tune the separation of charge carriers and the efficiency of photocatalytic reactions by changing the composition

(here: pH) of the electrolyte. Since the presence of surface defects and anisotropic charging behavior of various planes of a particle is very common, we expect the phenomena described here will be generically applicable to other semiconductor materials that display facet-selective deposition of metal and metal oxides.

Conflicts of interest

There are no conflicts to declare.

Acknowledgements

We thank Dr Fei Liu, Dr Chamy Mahendran, Dr Kasper Wenderich, Kai Han and Mark Smithers for assistance in measurements and helpful discussions. This work was jointly supported by the National Natural Science Foundation of China (No. 51672258 and 51572246), and the Fundamental Research Funds for the Central Universities (2652015296), of the China Scholarship Council.

Notes and references

1 K. Maeda, K. Teramura, D. Lu, T. Takata, N. Saito, Y. Inoue and K. Domen, *Nature*, 2006, **440**, 295.
2 M. R. Hoffmann, S. T. Martin, W. Choi and D. W. Bahnemann, *Chem. Rev.*, 1995, **95**, 69–96.
3 Z. Zou, J. Ye, K. Sayama and H. Arakawa, *Nature*, 2001, **414**, 625–627.
4 S. Malato, P. Fernández-Ibáñez, M. I. Maldonado, J. Blanco and W. Gernjak, *Catal. Today*, 2009, **147**, 1–59.
5 D. S. Bhatkhande, V. G. Pangarkar and A. A. Beenackers, *J. Chem. Technol. Biotechnol.*, 2002, **77**, 102–116.
6 X. Wang, G. Baskaran, Z. Liu, J. Huijben, J. Yi, A. Annadi, A. R. Barman, A. Rusydi, S. Dhar and Y. Feng, *Nat. Commun.*, 2011, **2**, 188.
7 X. Wang, Q. Xu, M. Li, S. Shen, X. Wang, Y. Wang, Z. Feng, J. Shi, H. Han and C. Li, *Angew. Chem., Int. Ed.*, 2012, **51**, 13089–13092.
8 M. Ni, M. K. Leung, D. Y. Leung and K. Sumathy, *Renewable Sustainable Energy Rev.*, 2007, **11**, 401–425.
9 J. Yang, D. Wang, H. Han and C. Li, *Acc. Chem. Res.*, 2013, **46**, 1900–1909.
10 J. Li, L. Cai, J. Shang, Y. Yu and L. Zhang, *Adv. Mater.*, 2016, **28**, 4059–4064.
11 A. Kudo and Y. Miseki, *Chem. Soc. Rev.*, 2009, **38**, 253–278.
12 J. Zhang, Q. Xu, Z. Feng, M. Li and C. Li, *Angew. Chem., Int. Ed.*, 2008, **47**, 1766–1769.
13 G. Liu, C. Y. Jimmy, G. Q. M. Lu and H.-M. Cheng, *Chem. Commun.*, 2011, **47**, 6763–6783.
14 K. Wenderich and G. Mul, *Chem. Rev.*, 2016, **116**, 14587–14619.
15 G. W. Busser, B. Mei, P. Weide, P. C. K. Vesborg, K. Stührenberg, M. Bauer, X. Huang, M.-G. Willinger, I. Chorkendorff, R. Schlögl and M. Muhler, *ACS Catal.*, 2015, **5**, 5530–5539.
16 K. Han, T. Kreuger, B. Mei and G. Mul, *ACS Catal.*, 2017, **7**, 1610–1614.
17 K. Han, Y.-C. Lin, C.-M. Yang, R. Jong, G. Mul and B. Mei, *ChemSusChem*, 2017, **10**, 4510–4516.
18 L. Li, P. A. Salvador and G. S. Rohrer, *Nanoscale*, 2014, **6**, 24–42.
19 P. Zhou, H. Zhang, H. Ji, W. Ma, C. Chen and J. Zhao, *Chem. Commun.*, 2017, **53**, 787–790.
20 T. R. Gordon, M. Cargnello, T. Paik, F. Mangolini, R. T. Weber, P. Fornasiero and C. B. Murray, *J. Am. Chem. Soc.*, 2012, **134**, 6751–6761.
21 J. W. Bullard and M. J. Cima, *Langmuir*, 2006, **22**, 10264–10271.
22 X. Wu, Y. H. Ng, L. Wang, Y. Du, S. X. Dou, R. Amal and J. Scott, *J. Mater. Chem. A*, 2017, **5**, 8117–8124.
23 H. Zhang, Y. Yang, Z. Zhou, Y. Zhao and L. Liu, *J. Phys. Chem. C*, 2014, **118**, 14662–14669.
24 L. Zhang, W. Wang, S. Sun, D. Jiang and E. Gao, *Appl. Catal., B*, 2015, **162**, 470–474.
25 R. Li, F. Zhang, D. Wang, J. Yang, M. Li, J. Zhu, X. Zhou, H. Han and C. Li, *Nat. Commun.*, 2013, **4**, 1432.
26 D. Wang, H. Jiang, X. Zong, Q. Xu, Y. Ma, G. Li and C. Li, *Chem.–Eur. J.*, 2011, **17**, 1275–1282.
27 T. Ohno, K. Sarukawa and M. Matsumura, *New J. Chem.*, 2002, **26**, 1167–1170.
28 T. Tachikawa, S. Yamashita and T. Majima, *J. Am. Chem. Soc.*, 2011, **133**, 7197–7204.
29 N. Wang, D. Wang, M. Li, J. Shi and C. Li, *Nanoscale*, 2014, **6**, 2061–2066.
30 Y. P. Xie, G. Liu, L. Yin and H.-M. Cheng, *J. Mater. Chem.*, 2012, **22**, 6746–6751.
31 J. L. Giocondi, P. A. Salvador and G. S. Rohrer, *Top. Catal.*, 2007, **44**, 529–533.
32 L. Mu, Y. Zhao, A. Li, S. Wang, Z. Wang, J. Yang, Y. Wang, T. Liu, R. Chen and J. Zhu, *Energy Environ. Sci.*, 2016, **9**, 2463–2469.
33 J. Zhu, F. Fan, R. Chen, H. An, Z. Feng and C. Li, *Angew. Chem., Int. Ed.*, 2015, **54**, 9111–9114.
34 W. Chen, Q. Kuang, Q. Wang and Z. Xie, *RSC Adv.*, 2015, **5**, 20396–20409.
35 K. Wenderich, A. Klaassen, I. Siretanu, F. Mugele and G. Mul, *Angew. Chem., Int. Ed.*, 2014, **53**, 12476–12479.
36 Z. Zhang and J. T. Yates Jr, *Chem. Rev.*, 2012, **112**, 5520–5551.
37 A. J. Nozik and R. Memming, *J. Phys. Chem.*, 1996, **100**, 13061–13078.
38 Y. Matsumoto, T. Yoshikawa and E. i. Sato, *J. Electrochem. Soc.*, 1989, **136**, 1389–1391.
39 M. Gratzel, *Nature*, 2001, **414**, 338.
40 R. Beranek, *Adv. Phys. Chem.*, 2011, **2011**, 786759.
41 C. Ding, X. Zhou, J. Shi, P. Yan, Z. Wang, G. Liu and C. Li, *J. Phys. Chem. B*, 2015, **119**, 3560–3566.
42 M. Batzill, *Energy Environ. Sci.*, 2011, **4**, 3275–3286.
43 C. Minero, in *Environmental Photochemistry Part III*, Springer, 2013, pp. 23–44.
44 C. Guillard, E. Puzenat, H. Lachheb, A. Houas and J.-M. Herrmann, *Int. J. Photoenergy*, 2005, **7**, 1–9.

45 M. Kibria, S. Zhao, F. Chowdhury, Q. Wang, H. Nguyen, M. Trudeau, H. Guo and Z. Mi, *Nat. Commun.*, 2014, **5**, 3825.
46 M. Kibria, F. Chowdhury, S. Zhao, B. AlOtaibi, M. Trudeau, H. Guo and Z. Mi, *Nat. Commun.*, 2015, **6**, 6797.
47 W. E. Farneth, R. S. McLean, J. D. Bolt, E. Dokou and M. A. Barteau, *Langmuir*, 1999, **15**, 8569–8573.
48 P. Morris Hotsenpiller, J. Bolt, W. Farneth, J. Lowekamp and G. Rohrer, *J. Phys. Chem. B*, 1998, **102**, 3216–3226.
49 G. Dong and L. Zhang, *J. Phys. Chem. C*, 2013, **117**, 4062–4068.
50 E. M. Sabio, M. Chi, N. D. Browning and F. E. Osterloh, *Langmuir*, 2010, **26**, 7254–7261.
51 L. Ye, L. Tian, T. Peng and L. Zan, *J. Mater. Chem.*, 2011, **21**, 12479–12484.
52 J. Wang, Y. Yu and L. Zhang, *Appl. Catal., B*, 2013, **136**, 112–121.
53 H. Cheng, B. Huang and Y. Dai, *Nanoscale*, 2014, **6**, 2009–2026.
54 H. Li, J. Shang, Z. Ai and L. Zhang, *J. Am. Chem. Soc.*, 2015, **137**, 6393–6399.
55 W. Zhang, Q. Zhang and F. Dong, *Ind. Eng. Chem. Res.*, 2013, **52**, 6740–6746.
56 X. Zhang, Z. Ai, F. Jia and L. Zhang, *J. Phys. Chem. C*, 2008, **112**, 747–753.
57 D. Zhang, J. Li, Q. Wang and Q. Wu, *J. Mater. Chem. A*, 2013, **1**, 8622–8629.
58 D. Wu, L. Ye, H. Y. Yip and P. K. Wong, *Catal. Sci. Technol.*, 2017, **7**, 265–271.
59 Y. Guo, Y. Zhang, N. Tian and H. Huang, *ACS Sustainable Chem. Eng.*, 2016, **4**, 4003–4012.
60 F. Liu, C. Zhao, F. Mugele and D. van den Ende, *Nanotechnology*, 2015, **26**, 385703.
61 A. Klaassen, F. Liu, D. Van den Ende, F. Mugele and I. Siretanu, *Nanoscale*, 2017, **9**, 4721–4729.
62 C. Zhao, D. Ebeling, I. Siretanu, D. van den Ende and F. Mugele, *Nanoscale*, 2015, **7**, 16298–16311.
63 H. Li, T. Hu, N. Du, R. Zhang, J. Liu and W. Hou, *Appl. Catal., B*, 2016, **187**, 342–349.
64 I. Siretanu, D. van den Ende and F. Mugele, *Nanoscale*, 2016, **8**, 8220.
65 L. Ye, Y. Su, X. Jin, H. Xie and C. Zhang, *Environ. Sci.: Nano*, 2014, **1**, 90–112.
66 D. S. Bhachu, S. J. Moniz, S. Sathasivam, D. O. Scanlon, A. Walsh, S. M. Bawaked, M. Mokhtar, A. Y. Obaid, I. P. Parkin and J. Tang, *Chem. Sci.*, 2016, **7**, 4832–4841.
67 P. Murphy and M. LaGrange, *Geochim. Cosmochim. Acta*, 1998, **62**, 3515–3526.
68 M. Casaletto, A. Longo, A. Martorana, A. Prestianni and A. Venezia, *Surf. Interface Anal.*, 2006, **38**, 215–218.
69 I. Siretanu, D. Ebeling, M. P. Andersson, S. S. Stipp, A. Philipse, M. C. Stuart, D. Van Den Ende and F. Mugele, *Sci. Rep.*, 2014, **4**, 4956.
70 X. Zhang, J. Qin, Y. Xue, P. Yu, B. Zhang, L. Wang and R. Liu, *Sci. Rep.*, 2014, **4**, 4596.
71 W. Yuan, Y. Zhou, Y. Li, C. Li, H. Peng, J. Zhang, Z. Liu, L. Dai and G. Shi, *Sci. Rep.*, 2013, **3**, 2248.